

# Hard superconducting gap and diffusion-induced superconductors in Ge-Si nanowires

Joost Ridderbos,<sup>1</sup> Matthias Brauns,<sup>1</sup> Jie Shen,<sup>2</sup> Folkert K. de Vries,<sup>2</sup> Ang Li,<sup>3</sup> Sebastian Kölling,<sup>3</sup> Marcel A. Verheijen,<sup>3</sup> Alexander Brinkman,<sup>1</sup> Wilfred G. van der Wiel,<sup>1</sup> Erik P. A. M. Bakkers,<sup>3</sup> and Floris A. Zwanenburg<sup>1,\*</sup>

<sup>1</sup>*MESA+ Institute for Nanotechnology, University of Twente,  
P.O. Box 217, 7500 AE Enschede, The Netherlands*

<sup>2</sup>*QuTech and Kavli Institute of Nanoscience, Delft University of Technology, 2600 GA Delft, The Netherlands*

<sup>3</sup>*Department of Applied Physics, Eindhoven University of Technology,  
Postbox 513, 5600 MB Eindhoven, The Netherlands*

(Dated: May 18, 2022)

We show a hard induced superconducting gap in a Ge-Si nanowire Josephson transistor up to in-plane magnetic fields of 250 mT, an important step towards creating and detecting Majorana zero modes in this system. A hard induced gap requires a highly homogeneous tunneling heterointerface between the superconducting contacts and the semiconducting nanowire. This is realized by annealing devices at 180 °C during which aluminium inter-diffuses and replaces the germanium in a section of the nanowire. Next to Al, we find a superconductor with lower critical temperature ( $T_C = 0.9$  K) and a higher critical field ( $B_C = 0.9 - 1.2$  T). We can therefore selectively switch either superconductor to the normal state by tuning the temperature and the magnetic field and observe that the additional superconductor induces a proximity supercurrent in the semiconducting part of the nanowire even when the Al is in the normal state. In another device where the diffusion of Al rendered the nanowire completely metallic, a superconductor with a much higher critical temperature ( $T_C = 2.9$  K) and critical field ( $B_C = 3.4$  T) is found. The small size of diffusion-induced superconductors inside nanowires may be of special interest for applications requiring high magnetic fields in arbitrary direction.

## INTRODUCTION

The discovery that Majorana fermions offer a route towards an inherently topologically protected fault-tolerant quantum computer [1–3] marked the beginning of a quickly growing field of research to achieve their experimental realization. Majoranas require a topological superconducting material, which in practice can be realized by coupling a conventional  $s$ -wave superconductor to a 1-dimensional nanowire with high spin-orbit coupling and  $g$ -factor [4–7]. Signatures of Majorana fermions are expected to arise as a conductance peak at zero bias and finite magnetic fields. The first reports showing these zero-bias conductance peaks in InAs and InSb nanowires [8–12] suffered from sizeable sub-gap conductivity attributed to inhomogeneities in the nanowire-superconductor interface [13, 14]. The resulting quasiparticle poisoning decoheres Majorana states since they will participate in braiding operations [15–17], and additionally obscure the Majorana signatures at zero energy. Strong efforts have been made to improve these interfaces, i. e., induce a hard gap, using epitaxially grown Al [18, 19] or specialized surface treatments methods [20, 21], resulting in much better resolved Majorana signatures [16, 22–24].

In contrast to the group III-V materials used in previous work, we use Ge-Si core-shell nanowires, a candidate for observing Majoranas [25, 26] for which interaction with a superconductor is still relatively unexplored [27–30]. These wires are predicted to have a strong first-order Rashba type spin-orbit coupling [31] which, together with the  $g$ -factor [32, 33], is tunable by elec-

tric fields. Our devices consist of a nanowire with highly transparent superconducting Al source and drain [29, 34] on an oxidised Si substrate and exhibit two highly interesting properties: we find a hard induced superconducting gap and we observe the presence of an additional superconductor in the nanowire channel.

In this work, we focus on two devices: device A, shown in Fig. 1a, is a Josephson field-effect transistor [29] with has an additional superconductor we call X1 with a critical temperature  $T_{C,X1} = 0.9$  K, lower than of our Al contacts ( $T_{C,Al} = 1.4$  K), but a much higher critical field on the order of 1 T. It furthermore shows a hard induced superconducting gap near depletion. In device B (see Fig. SI2a), Al has diffused through the entire nanowire channel, rendering it metallic. Here we identify another superconductor (X2), which has both a higher critical temperature  $T_{C,X2} = 2.9$  K and a much higher  $B_{C,X2} \approx 3.4$  T (see Table I) than that of the Al contacts.

In the first part of this paper, we investigate Device A using high-angle annular dark field (HAADF) - scanning transmission electron microscopy (STEM) in combination with energy-dispersive X-ray spectroscopy (EDX). We find strong indications that the additional superconductor, as well as the highly homogeneous superconductor-nanowire interface arises during the thermal annealing process where Al inter-diffuses with the material in the semiconducting nanowire. In the second part, we map the switching current  $I_{SW}$  as a function of critical field  $B_C$  and critical temperature  $T_C$  of device A and B, which clearly shows an additional superconducting phase in both devices. In the final part we investigate the hardness of the superconducting gap in-

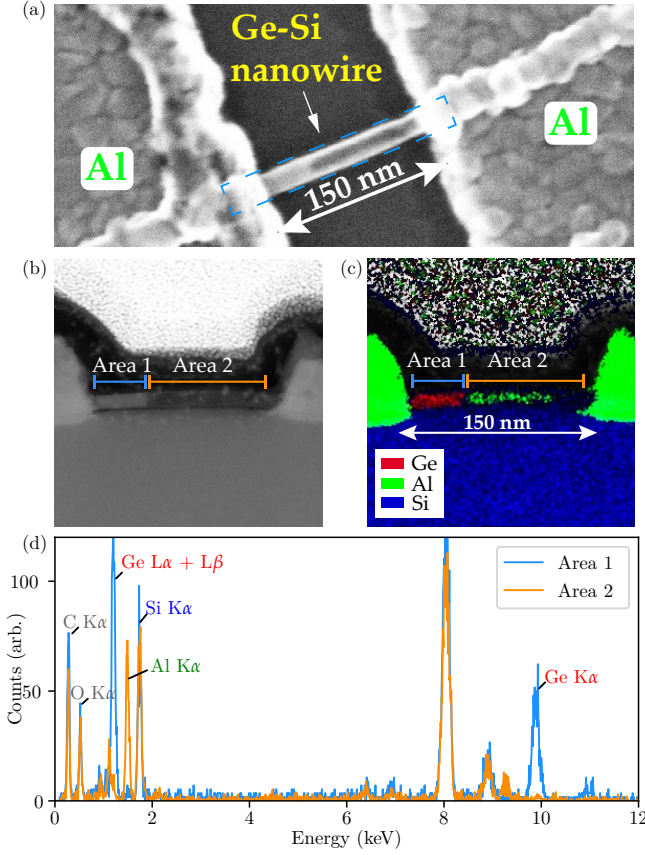


FIG. 1. **Al-Ge inter-diffusion in device A:** a) Top view SEM image of the device showing a Ge-Si nanowire between two Al contacts. In the right part of the nanowire, a slightly darker contrast is observed (see Supplementary Info Fig. S2 for SEM images showing this effect in several devices). The blue dashed line shows the approximate location of the TEM lamella. b) Cross-sectional HAADF-STEM image of the same device. The same contrast difference as in a) is observed. c) HAADF/STEM image with combined EDX data for elements Ge, Al and Si (see Supplementary Info Fig. S1 for separate images). d) EDX spectrum for Area 1 and Area 2 as defined in c).

duced in the semiconducting nanowire of device A, by means of electronic transport measurements near depletion [18, 21] and observe that the conductance in the gap is suppressed by a factor  $\sim 1000$ .

### AL-GE INTER-DIFFUSION

To gain insight in the effects of the annealing on the stoichiometric composition of the nanowire channel, a TEM lamella was made along the nanowire axes of device A as indicated in Figure 1a. This allows us to perform an analysis on the cross-section of the device as can be seen in Fig. 1b. In both Fig. 1a and b, a smaller region (Area 1) with higher contrast on the left, and a bigger region with lower contrast on the right (Area 2) can be

observed. Fig. 1c shows the resulting EDX signals in these regions for the elements Ge, Si and Al and we observe a clear distinction: in Area 1 we observe a strong Ge signal while in Area 2 the signal is dominated by Al.

In Figure 1d we show the integrated EDX spectra for both areas. When comparing the two areas, we observe that in Area 2 the Ge  $L\alpha$ , Ge  $L\beta$  and Ge  $K\alpha$  signals fall below the detection limit. As is the convention in EDX analysis,  $L$  and  $K$  denote the orbital to which an electron decays in a picture where  $K$ ,  $L$ , and  $M$  are the outer atomic orbitals, while  $\alpha$  and  $\beta$  indicate whether it decays from the first or second higher orbital. The Al  $K\alpha$  signal shows the opposite behavior, implying that Ge has been replaced by Al in Area 2 [35, 36]. The counts for elements O, C and Si remain equal in both areas (see also Supplementary Information Fig. S4). As we will discuss in the following section, the superconductor in Area 2 has profoundly different properties from the Al contacts and we therefore refer to it as X1. Inter-diffusion has also taken place below the left contact without reaching the channel, although this is not evident from the TEM data. Instead, we conclude this from transport data in the next section (Fig. 2 and Supplementary Information Fig. S5). As a sidenote, we cannot observe the effects of the inter-diffusion process on the Si shell, since the Si signal is dominated by the  $\text{SiO}_2$  that covers the substrate.

### TWO SUPERCONDUCTORS IN A NANOWIRE JOSEPHSON JUNCTION

In Fig. 2a we show a magneto-spectroscopy of device A, the Josephson junction: we plot the differential resistance  $\partial V_{\text{SD}}/\partial I_{\text{S}}$  versus the sourced current  $I_{\text{S}}$  and the out-of-plane magnetic field  $B_{\perp}$  (see inset Fig. 3b) while sweeping  $I_{\text{S}}$  from negative to positive current. The back-gate  $V_{\text{BG}}$  is fixed at  $-4.7$  V where multiple subbands contribute to transport and the junction is highly transparent [29]. The superconducting region (black) is bounded by  $I_{\text{R}} < I_{\text{S}} < I_{\text{SW}}$  with  $I_{\text{R}}$  the retrapping current at negative bias and  $I_{\text{SW}}$  the switching current at positive bias. Upon increasing  $B_{\perp}$  from 0,  $I_{\text{SW}}$  decreases gradually until aluminum becomes normal at the critical out-of-plane field  $B_{\text{C}\perp, \text{Al}} \approx 40$  mT after which a finite  $I_{\text{SW}}$  remains. For all  $B_{\perp}$ ,  $I_{\text{SW}} > I_{\text{R}}$  indicating our junction is slightly underdamped for this particular value of  $V_{\text{BG}}$  [29] (see Supplementary Information Fig. S5a for a gate-dependence of  $I_{\text{SW}}$  and  $I_{\text{R}}$ ).

When increasing  $B_{\perp}$  further in Fig. 3b,  $I_{\text{SW}}$  slowly decreases and finally disappears. The proximity-induced supercurrent above  $|B_{\text{C}\perp, \text{Al}}|$  implies the presence of a second superconducting material, X1, in or near the nanowire channel with a critical field  $B_{\text{C}\perp, \text{X1}} \approx 950$  mT. To confirm that our Al contacts are normal for  $B_{\perp} > |B_{\text{C}\perp, \text{Al}}|$ , we consider the background resistance  $R_{\text{B}}$  in

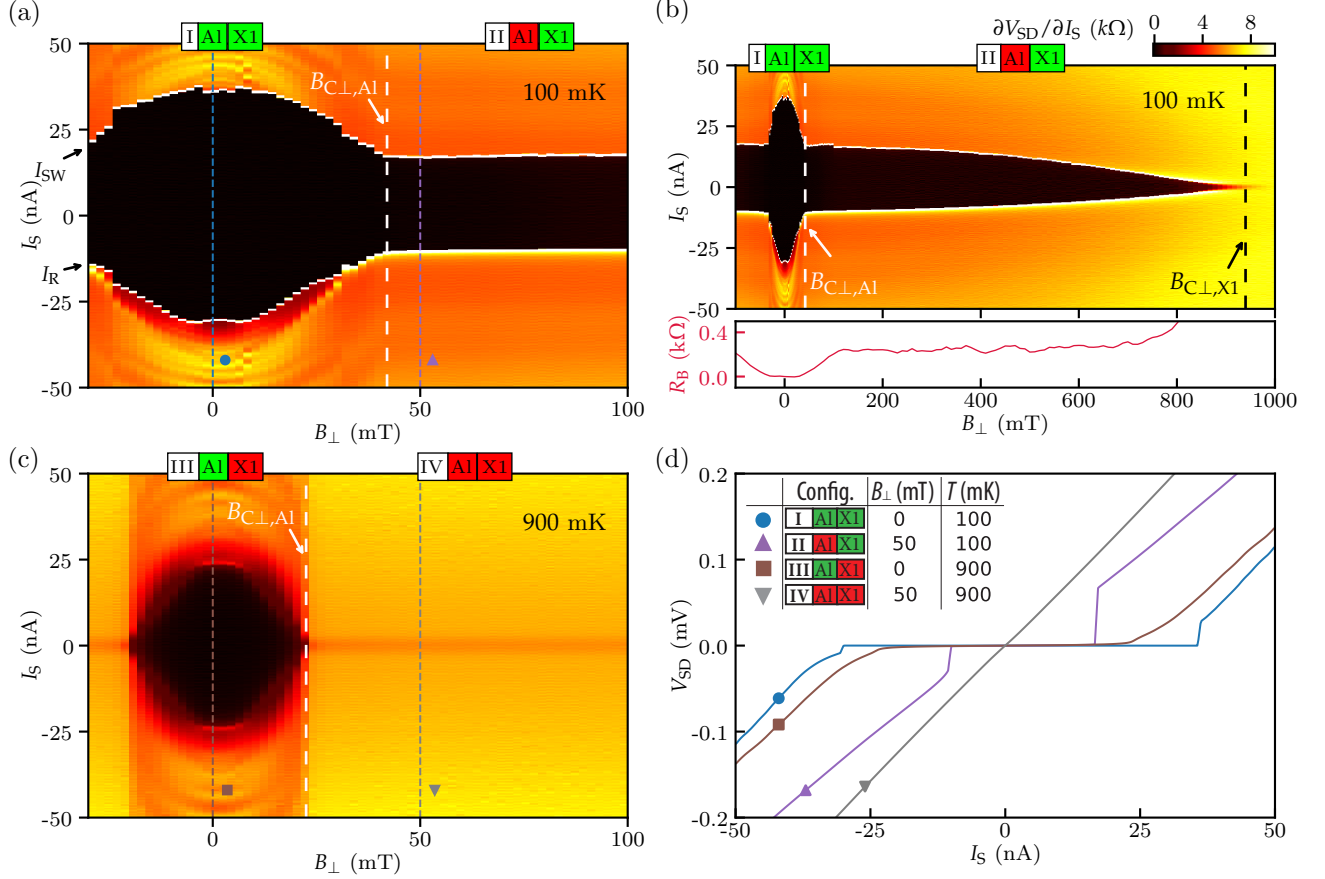


FIG. 2. **Device A: Josephson junction with two superconductors:** a) Differential resistance  $\partial V_{SD}/\partial I_S$  versus  $I_S$  and  $B_{\perp}$  taken at  $T = 100$  mK. Black region corresponds to superconductivity. The white dashed line indicates  $B_{C\perp,Al}$ . Arrows indicate  $I_{SW}$  and  $I_R$ . b) Top panel: Same as a) for a larger range of  $B_{\perp}$ . The vertical black dashed line indicates  $B_{C\perp,X1}$ . Bottom panel: Horizontal cross-section showing  $\partial V_{SD}/\partial I_S$  vs  $B_{\perp}$  taken at  $I_S = 0$ . The color scale also applies to a) and b). c) Same as a) taken at  $T = 900$  mK. d) Combinations of Al and X1 in the superconducting (green boxes) / normal (red boxes) state are numbered as configurations I-IV. Linecuts showing  $V_{SD}$  versus  $I_S$  taken for each configuration at the corresponding symbols in (a) and (c). Inset: table summarizing the configurations and values of  $B_{\perp}$  and  $T$  for the respective linecuts. In all figures  $V_{BG} = -4.7$  V and  $I_S$  is swept from negative to positive bias.

the superconducting region as a function of  $B_{\perp}$  in the bottom panel of Fig. 2b.  $R_B = 0$  for  $B_{\perp} < |B_{C\perp,Al}|$ , while for  $B_{\perp} > |B_{C\perp,Al}|$  the background resistance gradually increases to  $R_B \approx 0.25$  k $\Omega$  attributed to a normal series resistance of the Al contacts. Additionally, the out-of-plane critical field of a separately measured Al lead matches  $B_{C\perp,Al}$  (see Supplementary Information Fig. S3).

In Fig 2c we show a magneto-spectroscopy at 900 mK and observe that X1 is quenched for all  $B_{\perp}$ , while Al still induces a supercurrent for  $B_{\perp} < |25|$  mT. This shows that X1 has a lower  $T_C$  and a higher  $B_C$  than the Al contacts. Because X1 has a higher  $B_C$  and a lower  $T_C$  than Al, we can selectively switch either superconductor to the normal state, resulting in four possible device configurations **I-IV** as illustrated in Fig. 2 and summarized in the inset in Fig. 2d (a precise set of conditions for each configuration can be found in Supplementary

Information Table S1). Fig. 2d shows plots of  $V_{SD}$  versus  $I_S$  in all four configurations, clearly showing a supercurrent in configuration **II** where Al is normal and only X1 is superconducting. Since we observe a gate-tunable Josephson current even in configuration **II**, we conclude X1 is present on both sides of the Ge-Si segment (see Supplementary Information Fig. S5 for differential resistance maps versus backgate in all four configurations).

### JUNCTION $I_{SW}$ VERSUS $B$ AND $T$

Since for each superconductor the critical field and critical temperature are inter-dependent variables and may have a non-trivial relation, the boundaries of the configurations **I-IV** in terms of  $B_C$  and  $T_C$  cannot directly be deduced from the data in Fig. 2. We therefore collect  $I_{SW}$  versus  $B$  from magneto-spectroscopies for a large

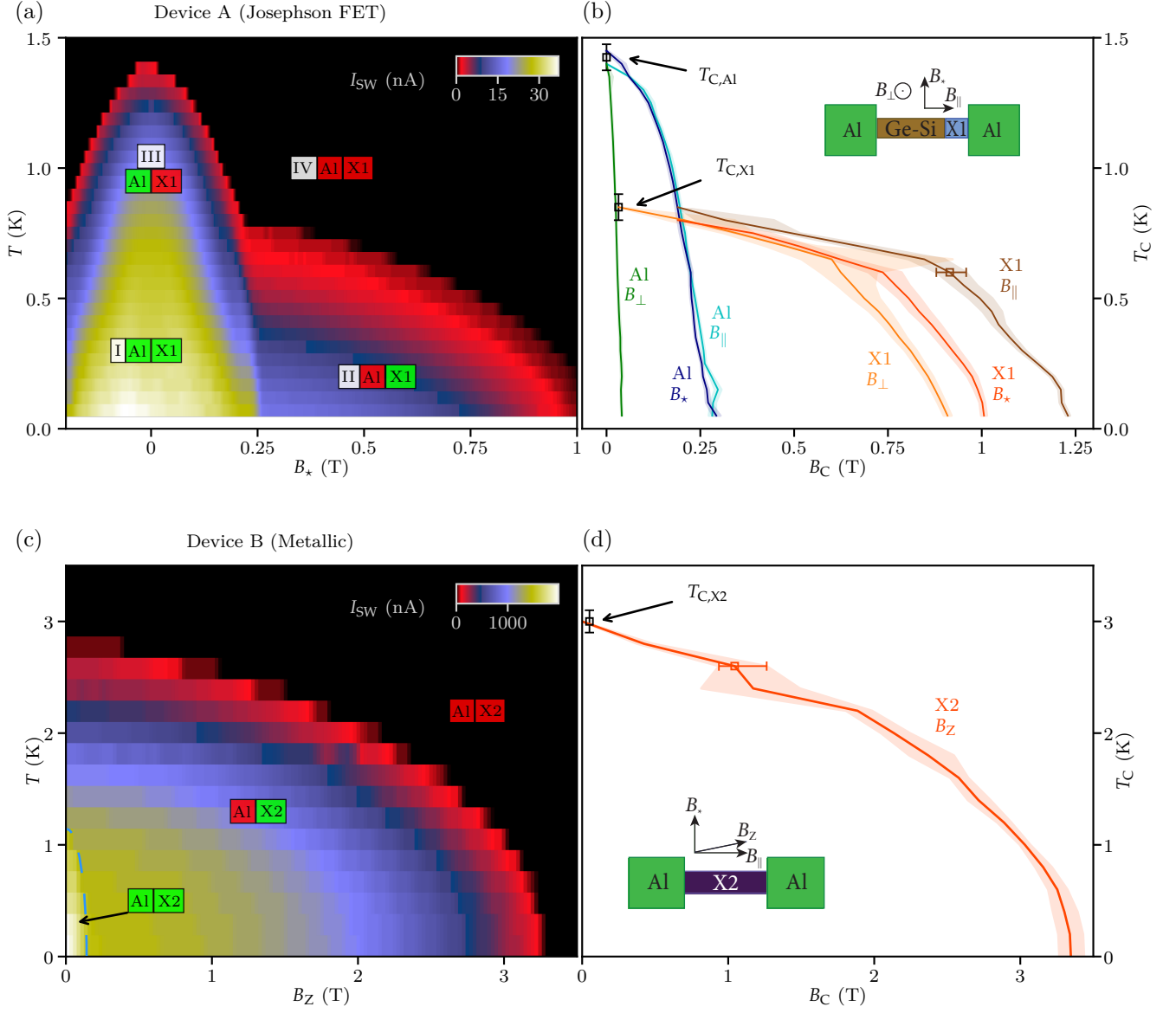


FIG. 3.  $I_{SW}$ ,  $T_C$  and  $B_C$  of a Josephson FET (device A) and a metallized nanowire device (device B): a)  $I_{SW}$  versus  $T$  and  $B_*$  for the Josephson FET (device A). The green (red) boxes indicate whether the material is superconducting (normal) and show the configurations I-IV as defined in the main text. b)  $T_C$  vs  $B_C$  for Al and X1 for three main field axis  $B_\perp$ ,  $B_\parallel$  and  $B_*$  as illustrated by the inset. Curves are extracted from plots such as a) (see main text). c)  $I_{SW}$  versus  $T$  and  $B_Z$  for the completely metallized nanowire (device B) consisting of alloy X2. The green (red) boxes indicate three possible configurations. For the configuration where Al is superconducting (for  $B_Z < 300$  mT and  $T < 1$  K) an enhancement of  $I_{SW}$  can be observed as denoted by the blue dotted line. d)  $T_C$  vs  $B_C$  for X2 extracted from c). Inset shows the in-plane  $B_Z$  field direction which is rotated  $\sim 10^\circ$  with respect to the nanowire.  $B_Z$  corresponds to the z-axis of the vector magnet, the only axis capable of fields  $> 1$  T. In both b) and d), the vertical error bar represents an uncertainty in  $T_C$  of 2 % and shaded areas are standard deviations in  $B_C$  from fits.

number of temperatures and the three main magnetic field axes  $B_*$ ,  $B_\perp$  and  $B_\parallel$  which are illustrated by the inset in Fig. 3b. For the in-plane field perpendicular to the nanowire,  $I_{SW}$  has two clearly distinct overlapping shapes as a function of  $T$  and  $B_*$  in Fig. 3a: The ‘peak’ extending to  $T \approx 1400$  mK at  $B = 0$  with a width of  $|B_*| \approx 250$  mT at  $T = 50$  mK is attributed to the superconducting state of Al, while the second shape (the

‘tail’), extending up to  $\sim 1000$  mT at  $T = 50$  mK, corresponds to the superconducting phase of X1. We can thus map the four configurations in the color plot on the  $T$  vs  $B_*$  axes.

We now extract both the  $T_C$ - $B_{C*,Al}$  and  $T_C$ - $B_{C*,X1}$  curves from Fig. 3a (see Supplementary Information section SII), i. e., the critical temperature - critical field relation for Al and X1, and plot them in Fig. 3b. We perform



TABLE I. Maximum values for  $T_C$ ,  $B_C$  of Al, X1 and X2 as determined in Fig. 3. We take  $T_{C,Al}(B_C = 0)$ ,  $T_{C,X1}(B_\perp = 50 \text{ mT})$  and  $B_C(T \approx 0)$  to obtain their respective maximum values. The BCS superconducting gap is determined as  $\Delta = 1.764k_B T_C$  [37].

	$T_C$ (K)	$\Delta$ ( $\mu\text{V}$ )	$B_{C\star}$ (mT)	$B_{C\perp}$ (mT)	$B_{C\parallel}$ (mT)
<b>Al</b>	$1.4 \pm 0.05$	$212 \pm 6$	$293 \pm 10$	$41 \pm 2$	$282 \pm 10$
<b>X1</b>	$0.9 \pm 0.05$	$133 \pm 8$	$1230 \pm 10$	$909 \pm 11$	$1010 \pm 20$

	$T_C$ (K)	$\Delta$ ( $\mu\text{V}$ )	$B_{C,Z}$ (T)
<b>X2</b>	$2.9 \pm 0.1$	$441 \pm 14$	$3.4 \pm 0.1$

the same procedure for field directions  $B_\perp$  and  $B_\parallel$  (see Supplementary Information Fig. S4 for  $I_{SW}$  versus  $T$  and  $B_\parallel$  and  $B_\perp$ ).

In Table. I we summarize the maximum  $T_C$ , the resulting superconducting gap  $\Delta$  and  $B_C$  in the three field directions for Al and X1. Comparing  $B_{C\perp,Al} = 41 \text{ mT}$  with  $B_{C\star,Al} = 293 \text{ mT}$  and  $B_{C\parallel,Al} = 282 \text{ mT}$  we notice a factor  $\sim 7$  difference. This strong anisotropy for the out-of-plane field direction is clearly present in the  $T_{C,Al}$ - $B_{C,Al}$  curves in Fig. 3b and is expected for the large aspect ratio of the 50 nm thick Al contacts.

The  $T_{C,X1}$ - $B_{C,X1}$  curves show a less prominent magnetic field anisotropy from which we can roughly deduce the shape of X1 by assuming that the normal surface of the material is inversely proportional to the critical field, i.e., a larger superconducting normal-surface requires expelling more flux [37]. Using the respective ratios of  $B_{C\star,X1}$ ,  $B_{C\perp,X1}$  and  $B_{C\parallel,X1}$  we observe that X1 is slightly elongated along the nanowire axis, reaffirming the hypothesis that X1 resides in the nanowire channel.

We now switch to the completely metallized device B where we believe Al has diffused completely through the channel, effectively making the nanowire a metallic superconductor. Fig. 3c shows  $I_{SW}$  vs  $T$  and  $B_Z$  where the corresponding  $T_{C,X2}$ - $B_{C,X2}$  relation in Fig. 3d is obtained by the previously mentioned polynomial fitting method. We see a critical temperature  $T_{C,X2} = 2.9 \text{ K}$  at  $B = 0$  and critical field  $B_{C,X2} = 3.4 \text{ T}$  at  $T = 50 \text{ mK}$ , both much higher than for X1 and the Al contacts. The switching current  $I_{SW} = 1.5 \mu\text{A}$  is two orders of magnitude higher compared to device A.

When comparing  $T_{C,X2} = 2.9 \text{ K}$  and  $B_{C,X2} = 3.4 \text{ T}$  with thin Al aluminium films [38], we observe X2 has equivalent properties of a  $\sim 3 \text{ nm}$  thick film (in parallel field) and we could conclude that X2 is simply a very small cylinder of aluminium inside the nanowire channel. However, for X1 with  $T_{C,X1} = 0.9 \text{ K}$  and  $B_{C,X1} \approx 1 \text{ T}$  an equivalent film thickness cannot be defined. Another possible origin of X1 is the formation of an alloy between Al and Ge (and possibly Si) where the ratio of semiconductor to Al results in signals that fall below the EDX detection limit. In literature, certain stoichiometric composi-

tions indeed result in a lower  $T_C$  than for pure Al [39, 40] and in fact, one can get alloys with a  $T_C$  ranging from 0.5 K up to 11 K by various methods [41–45]. The exact composition of both X1 and X2 therefore remains partly speculative.

To sum up, we observe X1 with  $T_{C,X1} = 0.9 \text{ K}$  in a Josephson junction and X2 with  $T_{C,X2} = 2.9 \text{ K}$  in a metallic device, showing that diffusion of Al into Ge-Si nanowires can give rise to different superconductors with a  $T_C$  lower and much higher than that of the Al contacts, both appear as a second superconductor in transport measurements. The high  $B_C$  of X1 and X2 in relation to their specific superconducting gaps makes them potentially interesting materials for superconductor-semiconductor devices where high magnetic fields are desired. A specific application could be the creation of Majorana fermions, either in this system [46] or in other materials where low  $g$ -factors would otherwise be limiting [47]. The challenge lies to both radially and longitudinally control Al-Ge inter-diffusion in the nanowire [36] to prevent metallizing the nanowire (see Fig. S2 for SEM images of several devices showing partially and fully metallized nanowire channels).

## TUNNELING REGIME OF THE JOSEPHSON FET

We now focus on device A and tune  $V_{BG}$  to a regime where the nanowire is near depletion. Fig. 4a shows the differential conductance  $\partial I_D / \partial V_{SD}$  versus the source-drain voltage  $V_{SD}$  and the backgate voltage  $V_{BG}$ . We notice a zero-bias conductance peak as the result of a finite Josephson current and a prominent multiple Andreev reflection (MAR) pattern showing as horizontal lines of increased conductance for  $V_{BG} = 3$  to 4 V. The reduced barrier transparency near depletion confines charges in the nanowire channel, and allows us to see odd and even charge occupation in a quantum dot in the wire [29] supported by a Kondo peak on the odd transitions [29, 48] (see Supplementary Information, Fig. S6). Above  $V_{BG} = 4.4 \text{ V}$ , the MAR and zero-bias peak disappear, while the onset of quasiparticle transport is visible at the induced gap at  $V_{SD} = \pm 2\Delta_{Al}$ . This trend is also present in the  $\partial I_D / \partial V_{SD}$  linecuts for  $V_{BG}$  between 4.35 and 4.80 V in Fig. 4b.

In Fig. 4a between  $V_{BG} = 4.2 \text{ V}$  and  $V_{BG} = 4.4 \text{ V}$  we observe a conductance peak in both bias directions smoothly moving from  $|V_{SD}| = \Delta_{Al}$  to  $|V_{SD}| = 2\Delta_{Al}$  when going from the odd to the even occupancy, which we attribute to an Andreev bound state (ABS). Additional evidence for an ABS presents itself in the form of a region of negative differential conductance in the odd occupancy between  $V_{SD} = \Delta_{Al}$  and  $V_{SD} = 2\Delta_{Al}$  [49, 50], as highlighted by the purple linecut at  $V_{BG} = 4.25 \text{ V}$  in

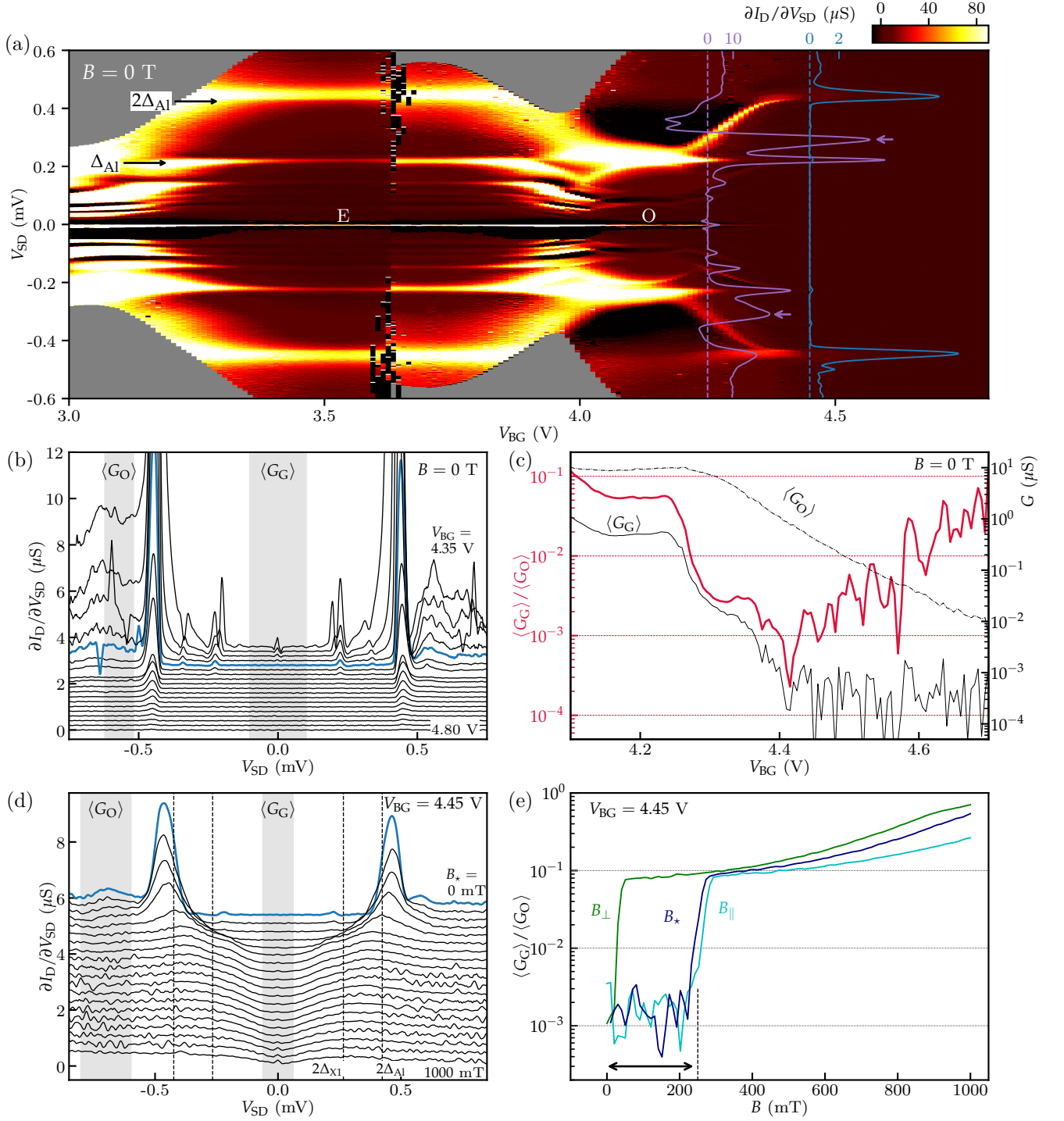


FIG. 4. **Hard superconducting gap in a Ge-Si nanowire Josephson FET (Device A):** a) Differential conductance  $\partial I_D / \partial V_{SD}$  vs  $V_{SD}$  and  $V_{BG}$ . Odd (O) and even (E) hole occupation are indicated. The first two MAR orders are indicated at  $V_{SD} = 2\Delta_{Al}$  and  $\Delta_{Al}$ . b) Vertical linecuts from a) showing  $\partial I_D / \partial V_{SD}$  vs  $V_{SD}$  at 50 mV interval in  $V_{BG}$ . Curves are offset by  $0.2 \mu S$ . c) Averaged in-gap conductance  $\langle G_G \rangle$  and outside-gap conductance  $\langle G_O \rangle$  and the ratio  $\langle G_G \rangle / \langle G_O \rangle$  versus  $V_{BG}$ .  $\langle G_G \rangle$  and  $\langle G_O \rangle$  are averaged over a range of  $V_{SD}$  for every  $V_{BG}$  as indicated by grey areas in (b)). d)  $\partial I_D / \partial V_{SD}$  vs  $V_{SD}$  for  $B_*$  from 0 to 1000 mT at 50 mT intervals. Curves are offset by  $0.3 \mu S$ . Dashed lines show the expected position of the quasiparticle peak for  $2\Delta_{Al}$  ( $2\Delta_{X1}$ ) at  $B = 0$ . e) Ratio  $\langle G_G \rangle / \langle G_O \rangle$  for the three main field axes  $B_\perp$ ,  $B_\parallel$  and  $B_*$  at  $V_{BG} = 4.45$  V (blue line in (a), (b) and (c)). Ranges in  $V_{SD}$  where  $\langle G_G \rangle$  and  $\langle G_O \rangle$  are extracted are shown as grey areas in c).

Fig. 3a. Tunnel spectroscopy on an ABS requires asymmetric opaque tunnel barriers where the most opaque barrier probes the ABS [48]. A barrier asymmetry in our devices can indeed be expected, since the final interface properties are determined by microscopic details on the Al-nanowire interface during annealing. For lower  $V_{BG}$  our barriers quickly become highly transparent [29] and we therefore only observe the ABS signature near depletion.

In contrast to the bias-symmetric MAR features, the asymmetric barriers show up in the intensity of the ABS signatures (see the arrows on the purple linecut in Fig. 4a). Depending on the bias direction, there are two different rate-determining tunnel sequences: (1) tunneling through an opaque barrier onto a single ABS or (2) tunneling from an ABS through an opaque barrier into the Fermi sea. Sequence (2) has a much higher tunnel probability than (1), which results in the observed asymmetry in conductance.

### HARD SUPERCONDUCTING GAP

A measure for the amount of quasiparticle states inside the gap, is the in-gap suppression of conductance also termed as the hardness of the induced gap. We therefore investigate the ratio  $\langle G_G \rangle / \langle G_O \rangle$  where  $\langle G_G \rangle$  ( $\langle G_O \rangle$ ) is an averaged conductance value inside (outside) the gap. Fig. 4c shows  $\langle G_G \rangle$ ,  $\langle G_O \rangle$  and the ratio  $\langle G_G \rangle / \langle G_O \rangle$  versus  $V_{BG}$  and we find the conductance is suppressed by a factor  $> 1000$  for  $V_{BG} \approx 4.4$  V, an order of magnitude higher than previously reported in this system [30]. Still, this should be considered as a lower limit, since  $\langle G_G \rangle / \langle G_O \rangle$  can be decreased due to several other reasons than quasiparticle poisoning: (1) for higher  $V_{BG}$ ,  $\langle G_G \rangle$  is limited by the noise floor of our measurement setup and does not further decrease. The decrease of  $\langle G_O \rangle$  now lowers the observed current suppression  $\langle G_G \rangle / \langle G_O \rangle$ . (2) MAR and the zero-bias peak, both characteristic for Josephson junctions, appear as conductance peaks inside the gap which leads to a decreased  $\langle G_G \rangle / \langle G_O \rangle$ . Devices where one of the contacts is normal will not exhibit these peaks and may therefore result in a lower ratio  $\langle G_G \rangle / \langle G_O \rangle$  and give a better approximation of the quasiparticle density in the gap. Because of this, we cannot directly compare the current suppression in our device (which has two superconducting contacts) with other work probing the induced gap using a single superconducting contact. Nevertheless, the high  $\langle G_G \rangle / \langle G_O \rangle$  ratio suggests that our semiconductor-nanowire interface homogeneity is comparable to InAs nanowire devices using epitaxial growth techniques [18] or specialized surface treatments [21].

We will now look at the magnetic field dependence of the hardness of the gap. We fix  $V_{BG}$  at 4.45 V and plot  $\partial I_D / \partial V_{SD}$  versus  $V_{SD}$  for several  $B_\star$  in Fig. 4d. For in-

creasing  $B_\star$ , the sharp quasiparticle peak at  $V_{SD} = 2\Delta_{Al}$  reduces in height and broadens up to  $B_{C_\star, Al} \approx 300$  mT. Above  $B_{C_\star, Al}$ , we enter configuration **II** where only X1 is superconducting but which fails to produce a clear second quasiparticle peak at  $\sim 2\Delta_{X1}$ . Instead, we see a ‘soft gap’ signature [13] persisting up to  $B_{C_\star, X1}$ .

In Fig 4e we plot the ratio  $\langle G_G \rangle / \langle G_O \rangle$  for the three main field directions. The initial ratio is  $\sim 1 \cdot 10^{-3}$  in configuration **I** as defined in Fig. 2 and the gap remains hard until we approach the critical field of Al for the respective field direction as summarized in Table I (See Supplementary Information Fig S8) for the corresponding differential conductance maps for all three main field axes). The highest field where the gap remains hard,  $B_\parallel \approx 250$  mT, is slightly lower than  $B_{C_\parallel, Al}$  because of the strongly reduced  $\Delta_{Al}$  at this field. The much softer gap in configuration **II** induced by X1 leads to a  $\langle G_G \rangle / \langle G_O \rangle \approx 1 \cdot 10^{-1}$  which gradually increases to 1 approaching  $B_{C, X1}$ . Another example of the change in transport properties when Al becomes normal is seen in Fig. 2a and Fig. 2c. Here, the fringes in the normal state attributed to multiple Andreev reflections (MAR) are only visible for  $B_\perp < B_{C_\perp, Al}$ . For  $B_\perp > B_{C_\perp, Al}$ , the absence of MAR suggests an increase of inelastic processes due to an ill-defined induced gap or a greatly increased quasiparticle poisoning rate.

The results in Fig. 4e show that the Al contacts needs to be superconducting in order to observe a hard gap. On the other hand, when only Al is superconducting, i.e., going from configuration **I** to **III** we observed no change in  $G_G$  that can be attributed to X1 becoming normal (see Supplementary Information, Fig. S7 for the temperature dependence of the differential conductance at  $V_{BG} = 4.45$  V and  $B = 0$ ). This suggests that X1 does not need to be a superconductor to observe a hard gap as long as the Al contacts proximise the entire junction. This is likely to happen, since the transparency between Al and X1 is high, and  $\Delta_{Al} > \Delta_{X1}$  indicating a coherence length for X1 comparable or larger than for Al, i.e., in the order of  $\mu m$  [51].

We now revisit Fig. 1b and c to investigate the interface between the X1 and the Ge-Si island. Even though our TEM and EDX resolution prohibits a conclusive statements about the interface properties on an atomic scale, the abrupt change in contrast suggests an upper limit for the interface width of a few nanometer. This observation is supported by work on pure Ge nanowires with Al contacts, where inter-diffusion due to Joule heating results in an atomically sharp interface between the Ge and the Al [35, 36] results in an atomically sharp interface between the Ge and the Al inside the wire. This type of interface would fit our observation of a hard gap which requires a defect-free highly homogeneous heterointerface [13], combined with the tunneling behavior achieved close to depletion. We therefore conclude that the diffusion-induced formation of X1 is essential for the hard induced gap [35, 36].

## CONCLUSION

We have shown that Ge-Si nanowire devices with Al contacts contain additional superconductors after annealing, caused by diffusion of Al into the nanowire channel. We identify two superconductors in two different devices: X1 is present in a Josephson FET and X2 resides in a metallic nanowire channel. Both X1 and X2 remain superconducting for magnetic fields much higher than the Al contacts which could be of potential interest for applications where proximity-induced superconductivity is required in high magnetic fields.

Close to depletion, the Josephson FET exhibits a hard superconducting gap where the in-gap conductance is suppressed by a factor  $\sim 1000$  up to magnetic fields of  $\sim 250$  mT in a superconductor-semiconductor-superconductor configuration. For higher fields, a soft gap remains up to the critical field of X1. We can selectively switch Al or X1 from the normal to the superconducting state and, together with the TEM and EDX analysis, we find that the homogeneous heterointerface between Ge-Si and X1 is essential in obtaining this hard gap. The next challenge is to more precisely control the diffusion of Al which would grant a highly promising system for observing Majorana zero modes [25].

## ACKNOWLEDGEMENTS

The authors acknowledge financial support from the Netherlands Organization for Scientific Research (NWO). E.P.A.M.B. acknowledges financial support through the EC Seventh Framework Programme (FP7-ICT) initiative under Project SiSpin No. 323841. Solliance and the Dutch province of Noord-Brabant are acknowledged for funding the TEM facility.

---

\* Corresponding author, e-mail: f.a.zwanenburg@utwente.nl

- [1] N. Read and D. Green, *Physical Review B* **61**, 10267 (2000).
- [2] S. Das Sarma, M. Freedman, and C. Nayak, *Physical Review Letters* **94**, 166802 (2005).
- [3] C. Nayak, S. H. Simon, A. Stern, M. Freedman, and S. Das Sarma, *Reviews of Modern Physics* **80**, 1083 (2008).
- [4] A. Y. Kitaev, *Physics Uspekhi* **44**, 130 (2000).
- [5] Y. Oreg, G. Refael, and F. von Oppen, *Physical Review Letters* **105**, 177002 (2010).
- [6] R. M. Lutchyn, J. D. Sau, and S. Das Sarma, *Physical Review Letters* **105**, 077001 (2010).
- [7] R. M. Lutchyn, E. P. A. M. Bakkers, L. P. Kouwenhoven, P. Krogstrup, C. M. Marcus, and Y. Oreg, *Nature Reviews Materials* **3**, 52 (2018).
- [8] A. Das, Y. Ronen, Y. Most, Y. Oreg, M. Heiblum, and H. Shtrikman, *Nature Physics* **8**, 887 (2012).
- [9] V. Mourik, K. Zuo, S. M. Frolov, S. R. Plissard, E. P. A. M. Bakkers, and L. P. Kouwenhoven, *Science* **336**, 1003 (2012).
- [10] E. J. H. Lee, X. Jiang, R. Aguado, G. Katsaros, C. M. Lieber, and S. De Franceschi, *Physical Review Letters* **109**, 186802 (2012).
- [11] A. D. K. Finck, D. J. Van Harlingen, P. K. Mohseni, K. Jung, and X. Li, *Physical Review Letters* **110**, 126406 (2013).
- [12] H. O. H. Churchill, V. Fatemi, K. Grove-Rasmussen, M. T. Deng, P. Caroff, H. Q. Xu, and C. M. Marcus, *Physical Review B* **87**, 241401 (2013).
- [13] S. Takei, B. M. Fregoso, H. Y. Hui, A. M. Lobos, and S. Das Sarma, *Physical Review Letters* **110**, 186803 (2013).
- [14] W. S. Cole, S. Das Sarma, and T. D. Stanescu, *Physical Review B* **92**, 174511 (2015).
- [15] D. Rainis and D. Loss, *Physical Review B - Condensed Matter and Materials Physics* **85**, 1 (2012).
- [16] A. P. Higginbotham, S. M. Albrecht, G. Kiršanskas, W. Chang, F. Kuemmeth, P. Krogstrup, T. S. Jespersen, J. Nygård, K. Flensberg, and C. M. Marcus, *Nature Physics* **11**, 1017 (2015).
- [17] S. M. Albrecht, E. B. Hansen, A. P. Higginbotham, F. Kuemmeth, T. S. Jespersen, J. Nygård, P. Krogstrup, J. Danon, K. Flensberg, and C. M. Marcus, *Physical Review Letters* **118**, 137701 (2017).
- [18] W. Chang, S. M. Albrecht, T. S. Jespersen, F. Kuemmeth, P. Krogstrup, J. Nygård, and C. M. Marcus, *Nature Nanotechnology* **10**, 232 (2015).
- [19] M. Kjaergaard, F. Nichele, H. J. Suominen, M. P. Nowak, M. Wimmer, A. R. Akhmerov, J. A. Folk, K. Flensberg, J. Shabani, C. J. Palmstrøm, and C. M. Marcus, *Nature Communications* **7**, 12841 (2016).
- [20] H. Zhang, Ö. Gül, S. Conesa-Boj, M. P. Nowak, M. Wimmer, K. Zuo, V. Mourik, F. K. de Vries, J. van Veen, M. W. A. de Moor, J. D. S. Bommer, D. J. van Woerkom, D. Car, S. R. Plissard, E. P. Bakkers, M. Quintero-Pérez, M. C. Cassidy, S. Koelling, S. Goswami, K. Watanabe, T. Taniguchi, and L. P. Kouwenhoven, *Nature Communications* **8**, 16025 (2017).
- [21] Ö. Gül, H. Zhang, F. K. De Vries, J. Van Veen, K. Zuo, V. Mourik, S. Conesa-Boj, M. P. Nowak, D. J. Van Woerkom, M. Quintero-Pérez, M. C. Cassidy, A. Geresdi, S. Koelling, D. Car, S. R. Plissard, E. P. Bakkers, and L. P. Kouwenhoven, *Nano Letters* **17**, 2690 (2017).
- [22] S. M. Albrecht, A. P. Higginbotham, M. Madsen, F. Kuemmeth, T. S. Jespersen, J. Nygård, P. Krogstrup, and C. M. Marcus, *Nature* **531**, 206 (2016).
- [23] M. T. Deng, S. Vaitiekė-Ūnas, E. B. Hansen, J. Danon, M. Leijnse, K. Flensberg, J. Nygård, P. Krogstrup, and C. M. Marcus, *Science* **354**, 1557 (2016).
- [24] Ö. Gül, H. Zhang, J. D. S. Bommer, M. W. A. de Moor, D. Car, S. R. Plissard, E. P. A. M. Bakkers, A. Geresdi, K. Watanabe, T. Taniguchi, and L. P. Kouwenhoven, *Nature Nanotechnology* **13**, 192 (2018).
- [25] F. Maier, J. Klinovaja, and D. Loss, *Physical Review B*

- 90, 195421 (2014).
- [26] M. Thakurathi, D. Loss, and J. Klinovaja, *Physical Review B* **95**, 155407 (2017).
- [27] J. Xiang, A. Vidan, M. Tinkham, R. M. Westervelt, and C. M. Lieber, *Nature Nanotechnology* **1**, 208 (2006).
- [28] Z. Su, A. Zarassi, B.-M. Nguyen, J. Yoo, S. A. Dayeh, and S. M. Frolov, arXiv:1610.03010 (2016).
- [29] J. Ridderbos, M. Brauns, J. Shen, F. K. de Vries, A. Li, E. P. A. M. Bakkers, A. Brinkman, and F. A. Zwanenburg, *Advanced Materials* **30**, 1802257 (2018).
- [30] F. K. de Vries, J. Shen, R. J. Skolasinski, M. P. Nowak, D. Varjas, L. Wang, M. Wimmer, J. Ridderbos, F. A. Zwanenburg, A. Li, S. Koelling, M. A. Verheijen, E. P. A. M. Bakkers, and L. P. Kouwenhoven, *Nano Letters* **18**, 6483 (2018).
- [31] C. Kloeffer, M. Trif, and D. Loss, *Physical Review B* **84**, 195314 (2011).
- [32] F. Maier, C. Kloeffer, and D. Loss, *Physical Review B* **87**, 161305 (2013).
- [33] M. Brauns, J. Ridderbos, A. Li, E. P. A. M. Bakkers, and F. A. Zwanenburg, *Physical Review B* **93**, 121408(R) (2016).
- [34] J. Ridderbos, M. Brauns, A. Li, E. P. A. M. Bakkers, A. Brinkman, W. G. van der Wiel, and F. A. Zwanenburg, Submitted.
- [35] S. Kral, C. Zeiner, M. Stöger-Pollach, E. Bertagnolli, M. I. den Hertog, M. Lopez-Haro, E. Robin, K. El Hajraoui, and A. Lugstein, *Nano Letters* **15**, 4783 (2015).
- [36] K. El Hajraoui, M. A. Luong, E. Robin, F. Brunbauer, C. Zeiner, A. Lugstein, P. Gentile, J. L. Rouvière, and M. Den Hertog, *Nano Letters* **19**, 2897 (2019).
- [37] M. Tinkham, *Introduction to Superconductivity* (1996).
- [38] R. Meservey and P. M. Tedrow, *Journal of Applied Physics* **42**, 51 (1971).
- [39] G. Deutscher and M. Rappaport, *Journal de Physique Lettres* **40**, 219 (1979).
- [40] J. Lesueur, L. Dumoulin, and P. Nédellec, *Solid State Communications* **66**, 723 (1988).
- [41] G. Deutscher, J. Farges, F. Meunier, and P. Nédellec, *Physics Letters A* **35**, 265 (1971).
- [42] C. C. Tsuei and W. L. Johnson, *Physical Review B* **9**, 4742 (1974).
- [43] W. Kuan, S. Chen, S. Yi, Z. Wang, C. Wu, and P. Garoche, *Journal of Low Temperature Physics* **46**, 237 (1982).
- [44] J. Chevrier, D. Pavuna, and F. Cyrot-Lackmann, *Physical Review B* **36**, 9115 (1987).
- [45] X.-X. Xi, Q.-Z. Ran, J.-R. Liu, and W.-Y. Guan, *Solid State Communications* **61**, 791 (1987).
- [46] F. Maier, T. Meng, and D. Loss, *Physical Review B* **90**, 155437 (2014).
- [47] T. D. Stanescu and S. Tewari, *Journal of Physics: Condensed Matter* **25**, 233201 (2013).
- [48] B.-K. Kim, Y.-H. Ahn, J.-J. Kim, M.-S. Choi, M.-H. Bae, K. Kang, J. S. Lim, R. López, and N. Kim, *Physical Review Letters* **110**, 076803 (2013).
- [49] J.-D. Pillet, C. H. L. Quay, P. Morfin, C. Bena, A. L. Yeyati, and P. Joyez, *Nature Physics* **6**, 965 (2010).
- [50] J. Gramich, A. Baumgartner, and C. Schönenberger, *Physical Review B* **96**, 1 (2017).
- [51] R. Gross and A. Marx, *Applied superconductivity*, Vol. 1 (2005) p. 480.

## Supplementary Information

### SI. FABRICATION

Ge-Si core-shell nanowires are deposited on a  $p^{++}$  doped Si substrate covered with 100 nm  $\text{SiO}_2$  and contacted after AFM imaging. Source and drain contacts are defined using electron-beam lithograph and after developing, a 3 second buffered hydrofluoric acid (12.5 %) dip is performed to remove native  $\text{SiO}_2$  from the Si shell of the nanowire. The contacts are metallized using electron-beam evaporation of Al, resulting in a 150 nm nanowire channel. As a last step, devices are annealed for 10 minutes on a hotplate in ambient at  $180^\circ\text{C}$  during which Al diffuses into the wire. As a result, a drop in room temperature resistance from several  $\text{M}\Omega$  to several  $\text{k}\Omega$  was observed for  $\sim 80\%$  of devices.

In total, 7 out of 15 devices tested at low temperature showed a supercurrent with 4 devices showing a superconducting phase with a  $T_C$  between 600 and 900 mK, comparable to X1. Three devices showed a metallized nanowire with comparable  $I_{\text{SW}}$  to device B, we have no information on their respective  $T_C$  or  $B_C$ .

### SII. EXTRACTION OF $T_C$ - $B_{C\star}$ CURVES

Here we explain how the  $T_C$ - $B_{C\star}$  curves of Fig. 3b in the main text were generated. We define  $B_{C\star, \text{Al}}$  ( $B_{C\star, \text{X1}}$ ) as the field where Al (X1) no longer induces a supercurrent, i.e., we no longer observe a  $I_{\text{SW}}$ . In Fig. 3a we cannot directly observe  $B_{C\star, \text{Al}}$  for  $0 > T > 800$  mK where the ‘peak’ of Al and the ‘tail’ of X1 overlap (for  $230 < B_\star < 300$  mT) and we therefore use the following method: (1) For all temperatures we take each individual  $I_{\text{SW}}$ - $B_\star$  curve, i.e., horizontal linecuts in Fig. 3a, (2) we select only  $I_{\text{SW}}$  where  $B_\star < B_{C\star, \text{Al}}$  (3) we fit  $I_{\text{SW}}$  to an empirical polynomial of



the form  $I_{\text{SW}}(B_{\star}) = aB_{\star}^4 + bB_{\star}^2 + c$  with  $a$  and  $b$  only allowed negative while  $c$  is always positive, (4) we find  $B_{\text{C}\star, \text{A1}}$  for each temperature as the roots of  $I_{\text{SW}}(B_{\star})$  (i. e., zero crossings). For X1 we use the same method except in (2) we select only  $I_{\text{SW}}$  for  $B_{\star} > B_{\text{C}\star, \text{A1}}$ .

### SIII. ADDITIONAL FIGURES AND TABLES

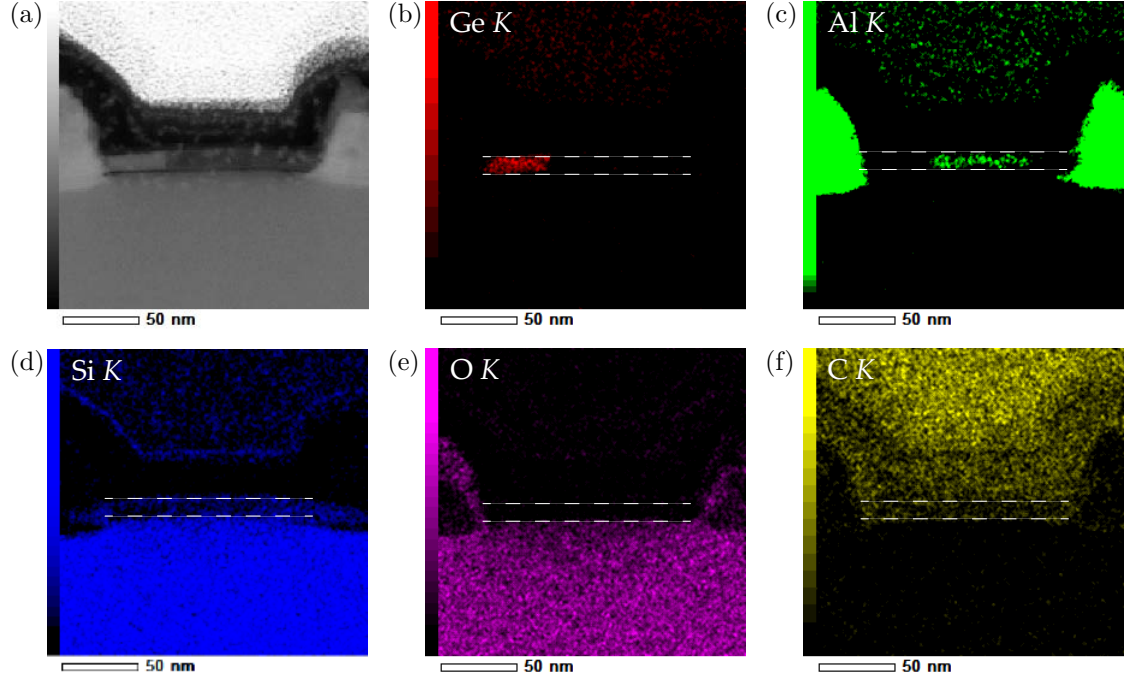


FIG. S1. **EDX maps of various elements of device A:** a) TEM image of device A, same as Fig. 1b in the main text. EDX map for Ge (b), Al (c), Si (d), O (e) and C (f). White dashed lines indicate the approximate position of the nanowire. (a), (b), (c) and (d) were used to construct Fig. 1c in the main text.

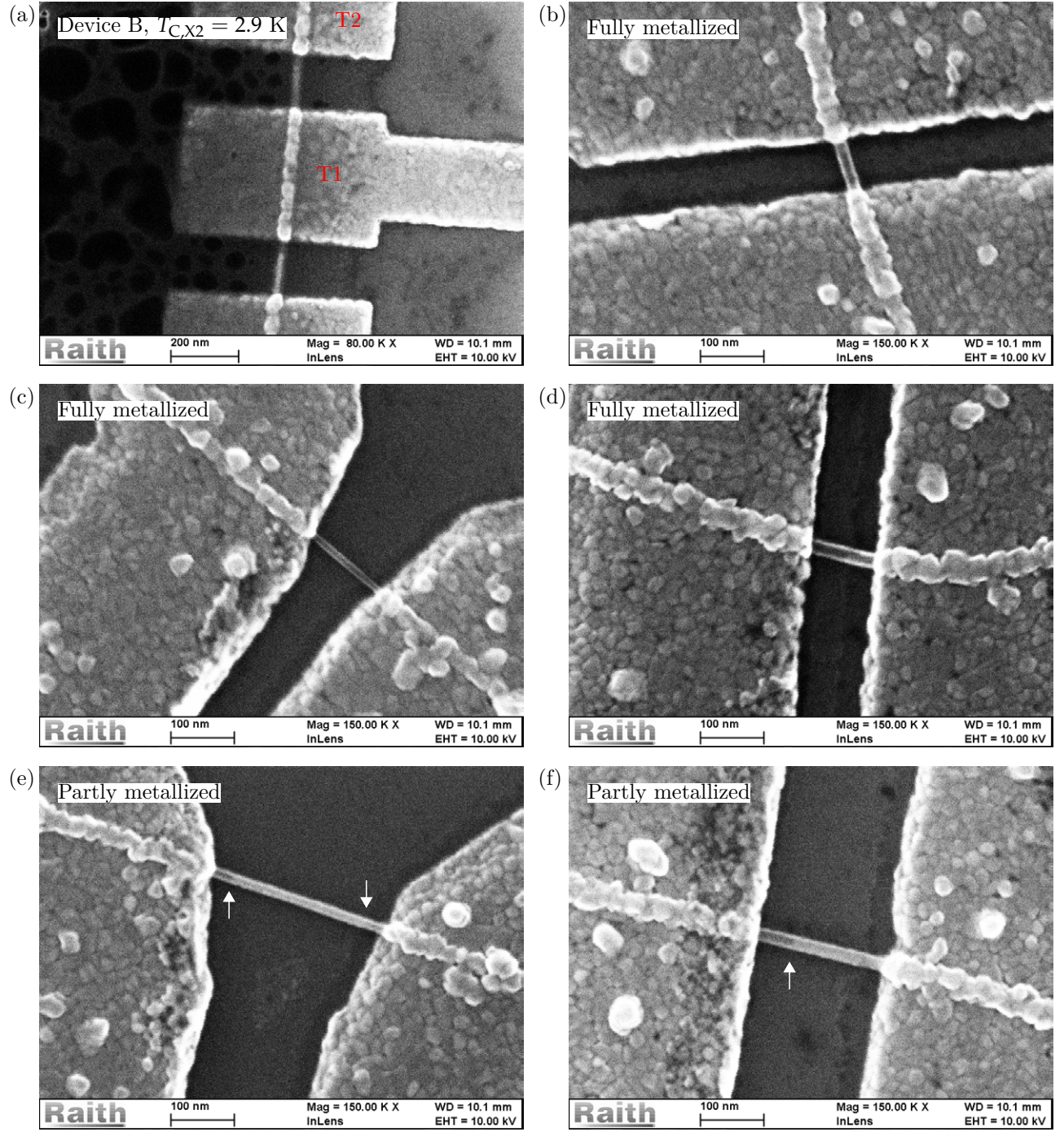


FIG. S2. **SEM images of devices:** a) SEM image of device B. Carbon contamination prevents a conclusive analysis of the Al-Ge inter-diffusion process. We suspect that the metallized nanowire segment is located between T1 and T2 based on the low contrast of the nanowire segment. b) Another metallized device exhibiting the same darkened color in the nanowire segment as in a), no additional superconducting phase was found in this device. c), d) More devices where the complete channel shows a low contrast for which we suspect they are fully metallized. e), f) Devices with a region of lower contrast close to the Al contacts, suspected due to partial metallization with the white arrows denoting the Al-Ge inter-diffusion front. Devices c) - f) were not measured. Other devices that were measured could not be imaged afterwards.

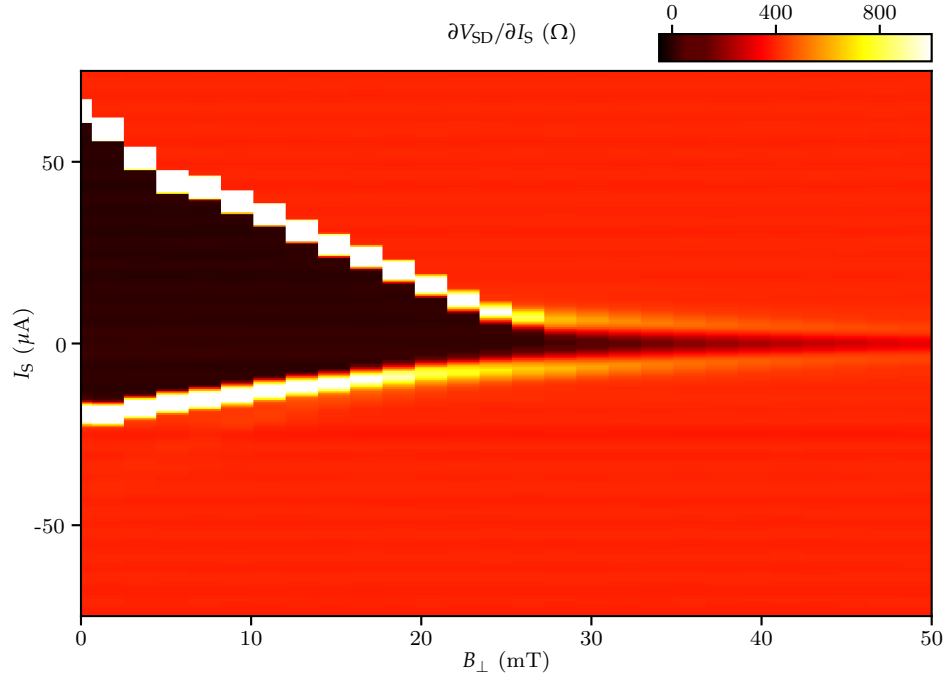


FIG. S3. **Al lead in an out-of-plane field:**  $\partial V_{SD}/\partial I_S$  vs  $I_S$  and  $B_{\perp}$ . The Al lead has a thickness of  $\sim 50$  nm and  $I_{SW}$  is determined by its smallest width of  $\sim 500$  nm running over a length of several  $\mu\text{m}$ . The black region denotes a supercurrent. The lead is measured in a 2-probe configuration and a series resistance of two times the line resistance is subtracted. Measurements are taken in the positive bias direction where the asymmetry in bias is attributed to local Joule heating.

TABLE S1. Configurations of device A with two superconducting phases and the corresponding conditions for the magnetic field  $\mathbf{B}$  and temperature  $\mathbf{T}$ , SC refers to superconductivity. The last column refers to the plots in Fig. 2d. For generality the field direction is removed from the subscripts.

Configuration	Superconducting	Normal state	Conditions	$I_{SW}$ and symbol
I	Al,X1		$\mathbf{B} < B_{C,Al}, B_{C,X1}$ & $\mathbf{T} < T_{C,X1}, T_{C,Al}$	$I_{SW} \approx 36$ nA ●
II	X1	Al	$B_{C,Al} < \mathbf{B} < B_{C,X1}$ & $\mathbf{T} < T_{C,X1}, T_{C,Al}$	$I_{SW} \approx 17$ nA ▲
III	Al	X1	$\mathbf{B} < B_{C,Al}, B_{C,X1}$ & $T_{C,X1} < \mathbf{T} < T_{C,Al}$	$I_{SW} \approx 24$ nA ■
IV		Al,X1	$\mathbf{B} > B_{C,X1}$ or $\mathbf{T} > T_{C,Al}$ or $B_{C,Al} < \mathbf{B} < B_{C,X1}$ & $T_{C,X1} < \mathbf{T} < T_{C,Al}$	$I_{SW} = 0$ ▼

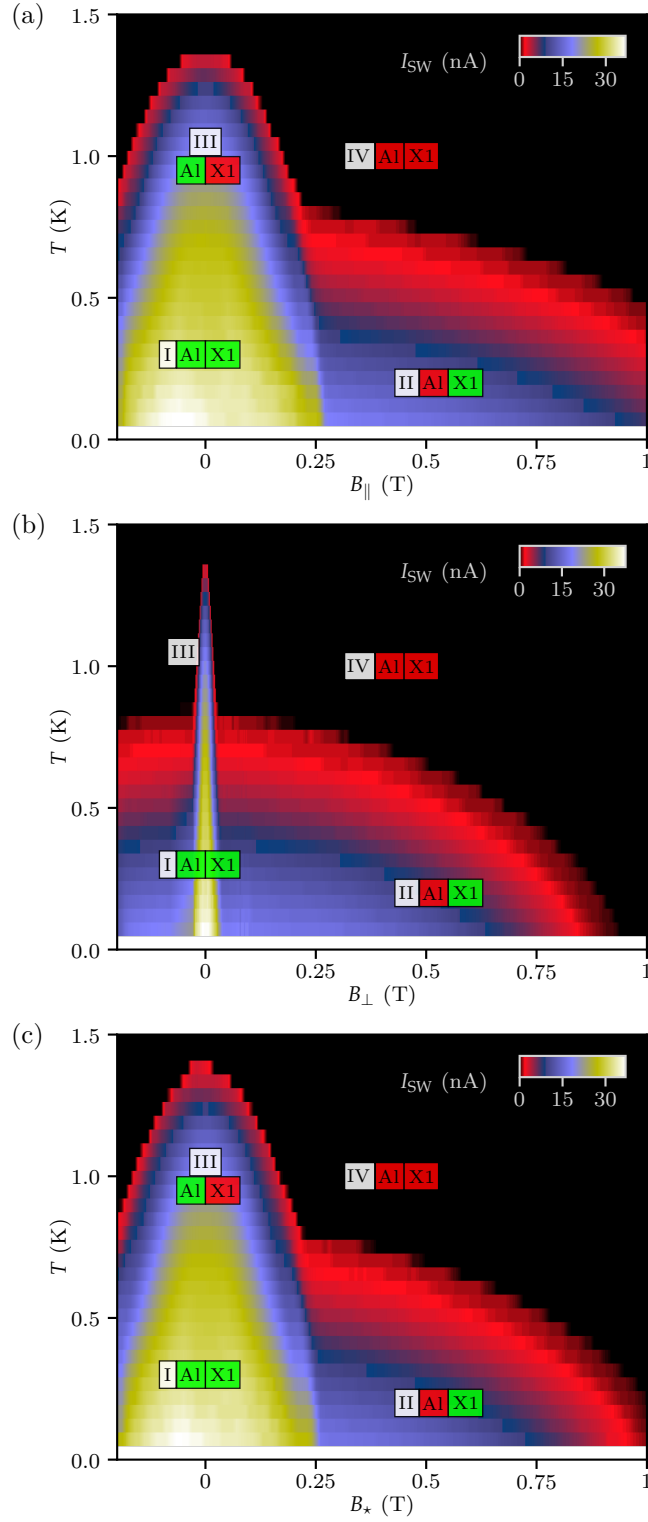


FIG. S4.  $I_{SW}$  vs  $T$  and  $B$  of Device A: Datasets were used to generate Fig. 3b in the main text as explained in section SII. a)  $I_{SW}$  vs  $B_{\parallel}$  and  $T$ , b)  $I_{SW}$  vs  $B_{\perp}$  and  $T$  and c)  $I_{SW}$  vs  $B_{\star}$  vs  $T$  (same as Fig. 3a in the main text). Configuration I-IV are denoted in all figures in which green indicates superconductivity while red indicates the normal state.



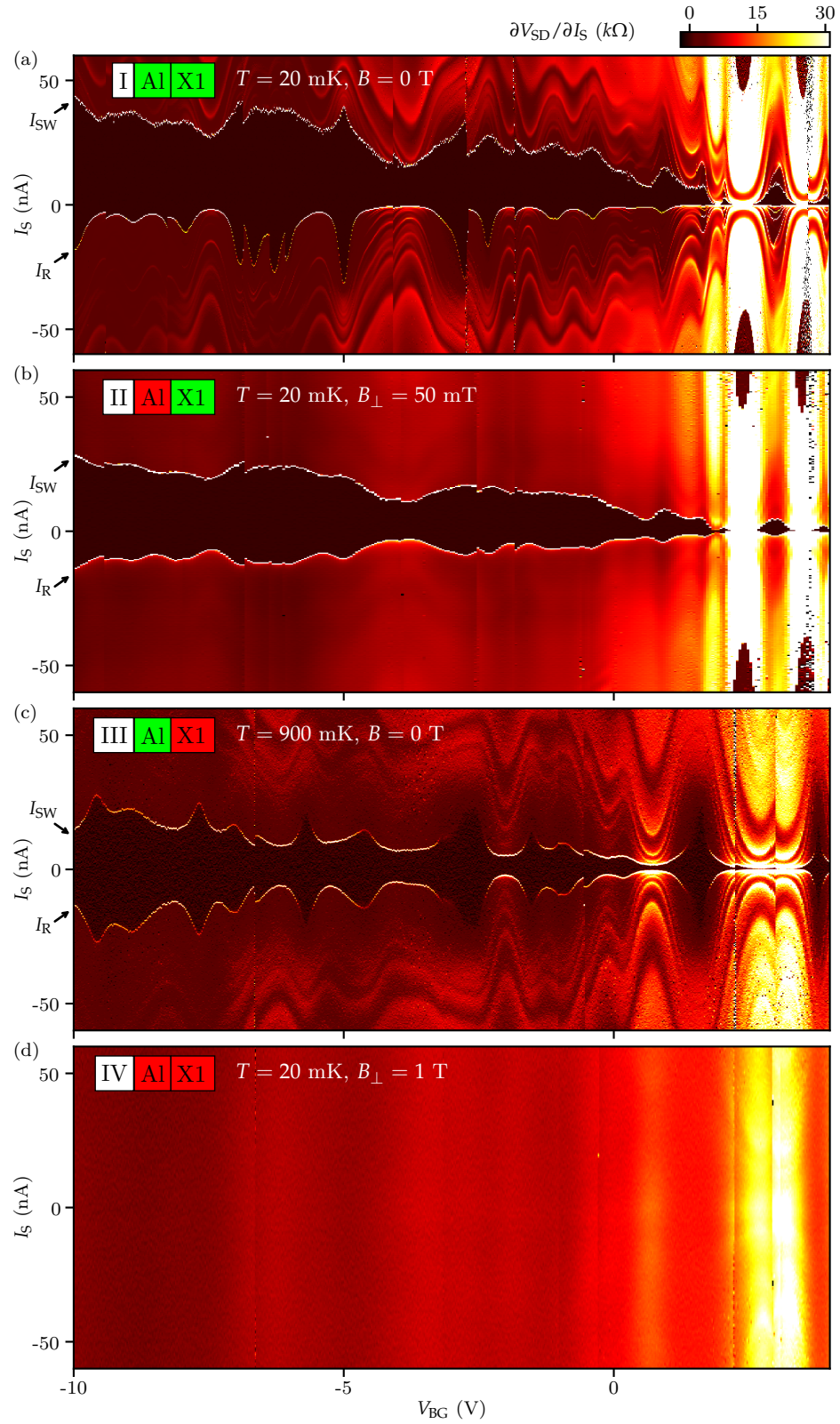


FIG. S5. **Backgate dependence for all four configurations:** All figures show  $\partial V_{SD}/\partial I_S$  vs  $I_S$  and  $V_{BG}$  with  $I_S$  measured from negative towards positive bias. a) Configuration **I** taken at  $T = 20$  mK and  $B = 0$  T. b) Configuration **II** taken at  $T = 20$  mK and  $B_{\perp} = 50$  mT. c) Configuration **III** taken at  $T = 900$  mK and  $B = 0$  T. d) Configuration **IV** taken at  $T = 20$  mK and  $B_{\perp} = 1$  T. In all figures,  $I_S$  was swept from negative to positive bias during measurement. a), b) and d) were taken during the same cooldown, all figures share the same color scale displayed in a). In a), b) and c),  $I_{SW}$  and  $I_R$  are denoted.

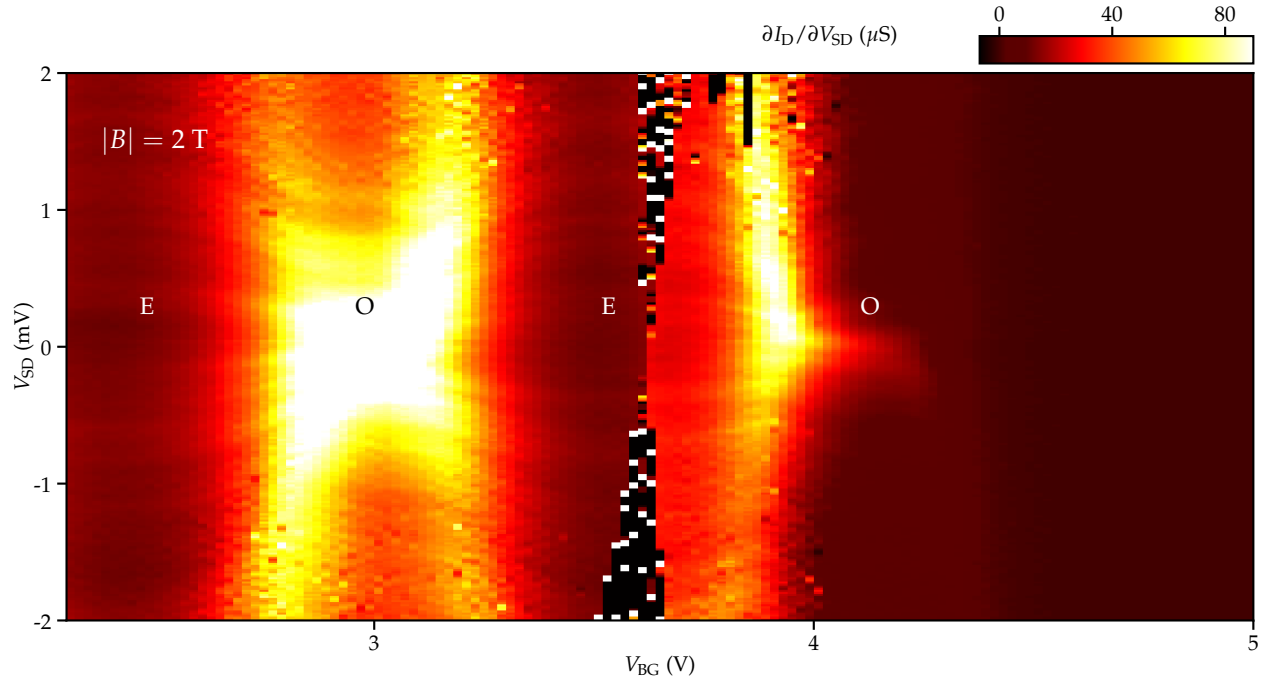


FIG. S6. **Kondo effect at finite magnetic field:**  $\partial I_D / \partial V_{SD}$  vs  $V_{SD}$  and  $V_{BG}$  for  $|B| = 2$  T. Odd (O) and even (E) hole occupation of the nanowire quantum dot is indicated. The Kondo effect is visible for odd occupation as increased conductance around  $V_{SD} = 0$ .

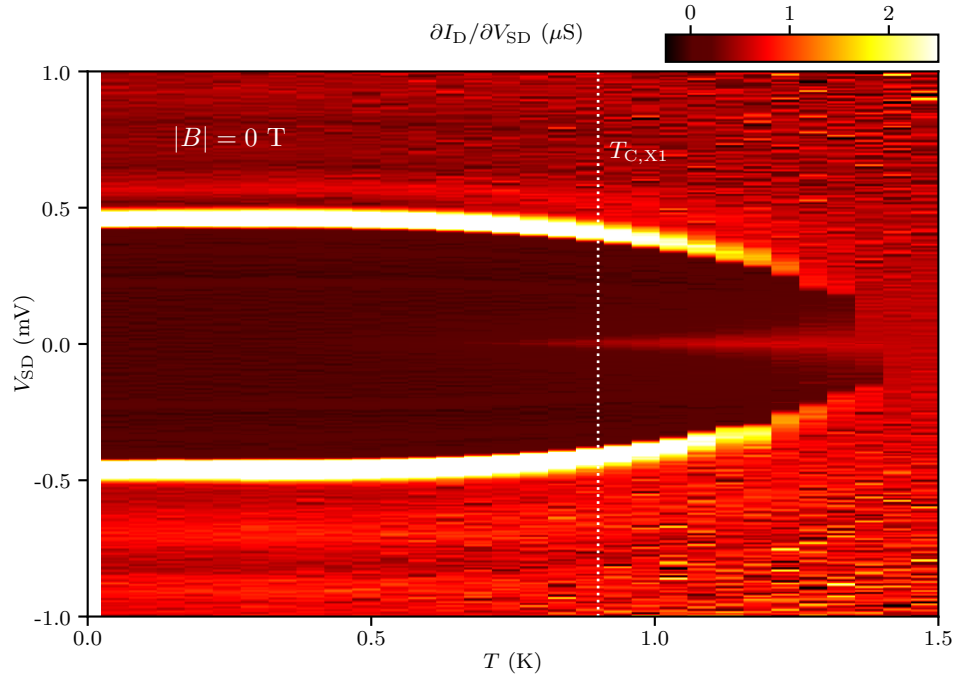


FIG. S7. **Induced superconducting gap versus  $T$ :**  $\partial I_D / \partial V_{SD}$  vs  $V_{SD}$  and  $T$  taken at  $V_{BG} = 4.45$  (blue dotted line in Fig. 4a.). The white dotted line indicates the critical temperature of X1  $T_{C,X1}$ . No abrupt change in conductance is observed above  $T_{C,X1}$ .

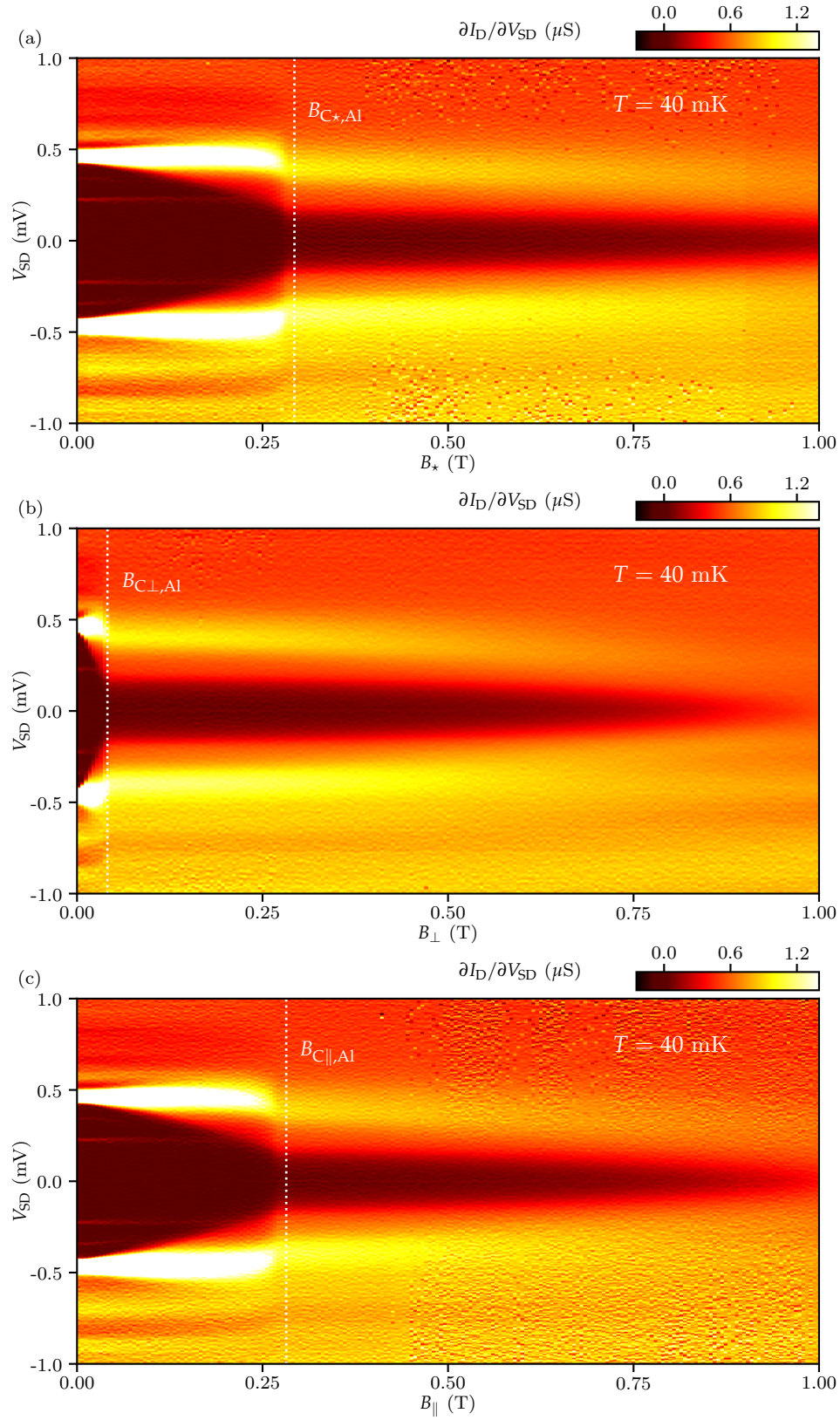


FIG. S8. **Superconducting gap versus  $B$ :** Datasets used to generate Fig. 4d and Fig. 4e in the main text, taken at  $V_{BG} = 4.45$  (blue dotted line in Fig. 4a). a)  $\partial I_D / \partial V_{SD}$  vs  $V_{SD}$  and  $B_*$ , the white dotted line indicates the critical field of Al  $B_{C*,Al}$ . b)  $\partial I_D / \partial V_{SD}$  vs  $V_{SD}$  and  $B_\perp$ , the white dotted line indicates  $B_{C\perp,Al}$ . c)  $\partial I_D / \partial V_{SD}$  vs  $V_{SD}$  and  $B_\parallel$ , the white dotted line indicates  $B_{C\parallel,Al}$ . Faint zero-bias peaks attributed to the Kondo effect appear only above  $B_{C*,Al}$ .